This document is confidential and is proprietary to the American Chemical Society and its authors. Do not copy or disclose without written permission. If you have received this item in error, notify the sender and delete all copies.

First-Principles Study on Optoelectronic Properties of Fedoped Montmorillonite Clay

Journal:	The Journal of Physical Chemistry Letters		
Manuscript ID	jz-2022-00697x.R1		
Manuscript Type:	Letter		
Date Submitted by the Author:	n/a		
Complete List of Authors:	Ghazanfari, Sarah; North Dakota State University Han, Yulun; North Dakota State University Xia, Wenjie; North Dakota State University, Department of Civil and Environmental Engineering Kilin, Dmitri; North Dakota State University, Chemistry and Biochemistry		

SCHOLARONE™ Manuscripts

First-Principles Study on Optoelectronic Properties of Fe-doped Montmorillonite Clay

Sarah Ghazanfari^a, Yulun Han^b, Wenjie Xia^{a, c*}, Dmitri S. Kilin^{b*}

^a Department of Civil, Construction, and Environmental Engineering, North Dakota State University, Fargo, ND 58108, United States

^b Department of Chemistry and Biochemistry, North Dakota State University, Fargo, ND 58108, United States

^c Materials and Nanotechnology, North Dakota State University, Fargo, ND 58108, United States

*To whom correspondence should be addressed.

Contact information:

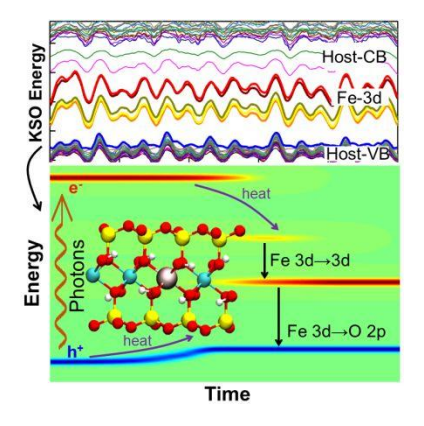
wenjie.xia@ndsu.edu (W.X.)

dmitri.kilin@ndsu.edu (D.K.)

ABSTRACT

A theoretical investigation is conducted to describe optoelectronic properties of Fe-doped montmorillonite nanoclay under low spin (LS), intermediate spin (IS), and high spin (HS). Ground state electronic properties are studied using spin-polarized density functional theory calculations. The nonradiative and radiative relaxation channels of charge carriers are studied by computing nonadiabatic couplings (NACs) using 'on-the-fly' approach from adiabatic molecular dynamics trajectories. The NACs are further processed using reduced density matrix approach with the Redfield formalism. The computational results are presented for electronic density of states, absorption spectra, charge carrier dynamics, and photoluminescence by comparing various spin multiplicities. Results on spin α and spin β components are independent and quite different due to the partial occupation of Fe 3d states. Overall, HS is the most stable with the largest Fe-O distances. One finds different nonradiative relaxation pathways in space and on time scale for electrons and holes. The Redfield PL reveals obvious Fe 3d-3d transitions for LS and IS.

TOC Graphic



Clay minerals are fine-grained soils that include a group of layered aluminum silicates or magnesium silicates, also known as phyllosilicates. Clay minerals have attracted widespread attention due to their different applications in industries such as drug-delivery systems,¹ catalyst supports,^{2,3} templates in organic synthesis,⁴ cosmetics,⁵ wastewater treatment,⁶, and petroleum industry.⁷ Understanding the optoelectronic properties of these types of minerals is a topic of great interest among researchers, especially in multidisciplinary fields such as chemistry, physics, engineering, and earth sciences.

Montmorillonite (MMT) with the chemical formula of Al₂Si₄O₁₀(OH)₂⁸ belongs to the smectite (2:1) clay minerals category that consists of one alumina octahedral (O) sheet sandwiched between two silica tetrahedral (T) sheets, T-O-T.⁹ These T-O-T layers are stacked in the c direction by relatively weak attractive van der Waals forces.¹⁰ Several isomorphic substitutions can happen that lead to the negative charge of layers, with the most common substitutions being Al³⁺ or Fe³⁺ to replace Si⁴⁺ in tetrahedral sheets and Mg²⁺or Fe³⁺ to replace Al³⁺ in octahedral sheets. Different interlayer counterions such as Na⁺, Mg²⁺, K⁺, Ca²⁺, and Cs⁺ can balance the negative charges induced by isomorphic substitution.^{9,11–17} In addition, it is found that Fe³⁺-MMT has enhanced adsorption of organics due to strong interactions such as ligand exchange, van der Waals forces, and H-bonding.¹⁸

Several experiments have been carried out to explore the physical and chemical features of MMT minerals. For instance, it was investigated that the number of exchangeable cations and hydration capability plays a governing role in the amount of absorbed water in MMT minerals.^{19,20} Moreover, studying of conductance behavior of ions with high valence in MMT reveals that these minerals can be used as promising solid electrolyte materials.²¹ There has been density functional theory (DFT)^{22,23} studies to explore the electronic properties of MMT minerals.^{24–28} For example,

with Perdew-Burke-Ernzerhof (PBE)²⁹ functional, a direct band gap of ~ 5.1 eV was reported for MMT.²⁸ Wungu et al. investigated Li migration from the interlayer into the vacant octahedral site of MMT.²⁴ The migration led to structural changes of MMT including reorientation of OH groups. The resulting Li-MMT exhibited charge transfer between Li and MMT and maintained insulating behavior. Despite extensive studies on electronic properties, optoelectronic properties of MMT with dopants are still worth investigating.

In this work, we carry out spin-polarized DFT calculations to study the ground state electronic properties for Fe-doped MMT with low spin (LS), intermediate spin (IS), and high spin (HS) multiplicities. A similar strategy has been adopted to study Russell–Saunders splitting for lanthanide ions doped in hexagonal (β)-NaYF₄ nanocrystals.³⁰ We then focus on the nonradiative relaxation of charge carriers and photoluminescence (PL) following photoexcitation. Such calculations require descriptions of nonadiabatic couplings (NACs) between electronic and nuclear degrees of freedom, which serve as parameters for the reduced density matrix (RDM) approach^{31,32} with the Redfield formalism.^{33,34} We aim to provide physical insight into the relaxation behavior of excitation energy for the system with different spin multiplicities where spin majority and spin minority components are studied independently. The results of this study on optoelectronic properties of Fe-doped MMT are expected to pave the way for the development of advanced application of clay minerals in various industries such as pharmaceutical and biomaterial applications.

Figure 1a-c shows the simplified schematic band diagram of Fe^{3+} doped MMT under different spin multiplicities. Ideally, one would expect the 'sandwich-like' electronic structures with valence band (VB) and conduction band (CB) mainly contributed by the transparent MMT host, and partially filled $3d^5$ orbitals from Fe^{3+} as fillings between VB and CB. The crystal field

splitting energy decreases from LS to HS. Photoexcitation can lead to several types of electronic transitions: VB \rightarrow CB, VB \rightarrow unoccupied Fe³⁺ 3 d^5 , occupied Fe³⁺ 3 d^5 \rightarrow unoccupied Fe³⁺ 3 d^5 .

The atomistic model in this work is derived from MMT with a formula of $Al_8Si_{16}O_{40}(OH)_8$. 35,36 One of the Al atoms in the octahedral sheet is substituted with a Fe atom. The resulting Fe-MMT structures are geometry optimized under LS, IS, and HS, respectively. During the geometry optimization, the ionic positions are allowed to change, while cell volumes and cell shapes are not. The optimized structure of HS Fe-MMT is shown in **Figure 1d**.

The total energies of optimized geometries for LS, IS, and HS are -598.460 (E – E_{HS} = 0.449), -598.462 (E – E_{HS} = 0.447), and -598.909 (E – E_{HS} = 0) eV, respectively. HS with the lowest total energy agrees with Hund's rule. One also finds structural changes from LS to HS. The average distances between Fe and six nearest neighboring O of optimized geometries for LS, IS, and HS are 1.96 Å, 2.00 Å, and 2.03 Å respectively (see supporting information Table S1). HS with the lowest total energy is found with the longest averaged Fe-O distances.

Figure 2a-c shows the partial density of states (PDOS) of optimized geometries for various spin multiplicities. In general, the Fe 3d states are found inside the gap of the host materials. From LS to HS, one starts to see the shifting of Fe 3d states for spin α components toward the VB edge of host materials, while the corresponding spin β components remain almost unchanged. As a result, one finds the increased degree of mixing of Fe 3d with O 2p orbitals in spin α from IS to HS. Substantial differences are observed between spin α and spin β components for Fe 3d states due to their partial occupations. By contrast, the spin α and spin β components are symmetric for regions in which Fe 3d orbitals make minimal contributions, as they are composed of filled s and p orbitals with spin-paired electrons of the host materials.

For LS, the frontier orbitals are composed of Fe 3d states and HO-LU gaps are ~ 1.52 and 0.41 eV for spin α and spin β , respectively. For spin α of IS, the frontier orbitals consist of mixed Fe 3d and O 2p orbitals and the HO-LU gap is ~ 0.74 eV. For spin β of IS, the frontier orbitals are contributed by Fe 3d orbitals and the HO-LU gap is ~ 0.72 eV. For spin α of HS, the HO orbital is composed of mixed Fe 3d and O 2p orbitals, whereas the LU orbital of Al, Si, and O s orbitals. The HO-LU gap of spin α is ~ 4.62 eV. For spin β of HS, the HO is contributed by O 2p orbitals, whereas the LU is by Fe 3d orbitals. The HO-LU gap of spin β is ~ 2.23 eV. One should bear in mind that the electronic structures are obtained using PBE functional.^{29,37} It is thus not surprising to learn that the band alignment is different from the one depicted in the schematic diagram in Figure 1. A band gap of 2.56 eV is observed for Na-MMT models by using generalized gradient approximation (GGA) with the exchange-correlation functional of Perdew-Wang 91^{38,39} where only Al3+/Mg2+ substitution took place in the octahedral sheets.25 Ferreira et al.40 calculated different band gaps for Fe-MMT-Na models utilizing various functionals and found band gaps of 1.4 eV by PBE, 7.0 eV by a modified Becke-Johnson (mBJ),^{29,41} and 4.3 eV by taking advantage of the hybrid Heyd-Scuseria-Ernzerhof (HSE06),⁴² with the latter comparable to experimental results. To more accurately describe the electronic structures of Fe-MMT for various spin multiplicities, one needs to use PBE + U (Hubbard correction)^{43,44} or hybrid functionals such as HSE06.42

Considering the 'sandwich-like' electronic structures are preserved for all spin β components, we will focus on these components for charge carrier dynamics and PL calculations. The results for spin α components can be found in supporting information. Note that we do not exclude the possibility of optical transitions that change the overall spin on the model e. g. from HS to LS. However, in this work, we perform spin-polarized DFT calculations to describe various

spin multiplicities of Fe-doped MMT. In this case, the spin is conserved and only α - α or β - β transitions are allowed. Non-collinear spin DFT calculations^{45–47} with spin-orbit coupling (SOC) effect that enables the spin-flip transitions would be a subject for future work. Such an implementation is available for the study of electronic structures of trivalent lanthanide ions doped β -NaYF₄ nanocrystals.⁴⁸

Figure 2d shows the computed absorption spectra of spin β components for LS, IS, and HS. The absorption corresponds to electronic transitions from occupied to unoccupied electronic states. The intensity is related to the transition dipole, which depends on the spatial overlap between electronic states under independent orbital approximations (IOAs).^{49,50} For LS and IS, features a-c and a'-b' are due to Fe d-d transitions, with the most intense transitions from HO-1 \rightarrow LU at 0.55 eV and HO \rightarrow LU at 0.72 eV, respectively. Such d-d transitions are not observed for HS, as all Fe 3d orbitals are unoccupied in spin β . The leading contributions for features d, f-g, c', e'-f', and a"-e" are from O $2p \rightarrow$ Fe 3d transitions. Features e and d' show transitions with characteristics of Fe 3d \rightarrow host s orbitals.

Next, one computes NACs using the 'on-the-fly' approach from adiabatic molecular dynamics trajectories. NACs are then processed using the autocorrelation function, the Fourier transform of which provides components of Redfield tensor according to the RDM approach with the Redfield formalism. The Redfield tensors control the level-to-level transition rates due to lattice vibrations. The details can be found in previous work.^{51,52} Note here NACs rely on solving Kohn-Sham equations using the projected augmented wave (PAW)⁵³ pseudopotentials. Recently, it has been shown that for transition metals the pseudopotentials can provide errors to the computed NAC vectors.⁵⁴ One should consider the calculation of NACs between all-electron wave functions when subshell d-electrons are involved in the transitions. Since we are conducting comparative

studies focusing on various spin multiplicities, the general trend of relaxations governed by NACs with PAW wave functions is expected to hold if we instead employ NACs with all-electron wave functions.

Figure 3 depicts the charge carriers' dynamics of spin β components for various spin multiplicities of Fe-MMT computed based on Redfield tensors. The left panels show isocontours of population density changes as a function of energy and time, whereas the middle panels show changes as a function of z-projection and time. The yellow, blue, and green colors indicate electron gain, loss, and no change compared to the equilibrium distributions, respectively. There is an initial photoexcitation, which creates a hot hole residing at HO-x and a hot electron at LU+y. This initial photoexcitation HO-x \rightarrow LU+y corresponds to the probable transitions with large oscillator strengths (strong peaks around 6 eV in **Figure 2d**). Here, HO-x orbitals are concentrated on O 2p orbitals, while LU+y on s orbitals of the host. Following the initial photoexcitation, hot charge carriers experience level-to-level transitions until the electron relaxes to LU and hole to HO by releasing excessive energy into heat.

Along the excited state trajectories, one finds several intermediate electronic states. Specifically, LU+1 and LU+2 are long-lived intermediate states of hot electrons, while HO-2 and HO-1 are long-lived intermediate states of hot holes, for LS and IS, respectively. Note that HO-1 to LU+2 and HO to LU+3 orbitals are five Fe 3*d* orbitals for LS and IS, respectively. For HS, only the hot electron shows a long-lived state at LU+3 corresponding to one of the Fe 3*d* orbitals, whereas HO-13 to HO are all localized on O 2*p*. The presence of intermediate electronic states is due to the inefficient charge migration in space.

The hole relaxation is found to be faster than the electron, see **Table 1**. With increasing spin multiplicities, one also finds an increase in both electron and hole relaxation rates. The fast

relaxation of hot hole for HS is due to an efficient relaxation channel among O 2p orbitals. The hot electron relaxation in space is similar for various spin multiplicities. The hot electron mainly locates at Si and O layers, which then relaxes to the Fe atom. By contrast, the hot hole relaxation reveals different patterns for various spin multiplicities. For LS, the hot hole mainly settles at the middle O layers, which then relaxes to the surface O layers and finally to the Fe atom. For IS, the hot hole mainly localizes at the middle O layers, which then relaxes to bottom two O layers and finally to the Fe atom. For HS, the hot hole mainly visits the middle O layers, which then relaxes to the surface O layers. The distinct relaxation pathways in space and on time scale of photoinduced carriers would make HS beneficial for photocatalysis.

In addition to nonradiative relaxation pathways, we investigate the competing radiative relaxation along the excited state trajectories. **Figure 4** shows time-integrated emission spectra of spin β components for various spin multiplicities of Fe-MMT. Here, the initial photoexcitation conditions are the same as in **Figure 3**. One finds the most intense peaks are attributed to LU \rightarrow HO transitions in accordance with Kasha's rule.⁵⁵ Together with LU \rightarrow HO transitions, one observes two other transitions, which are all characterized by Fe *d-d* transitions for LS (LU+1 \rightarrow HO ca. 1.58 eV and LU+1 \rightarrow LU ca. 1.17 eV) and IS (LU+2 \rightarrow HO ca. 1.98 eV and LU+2 \rightarrow LU+1 ca. 1.19 eV). In the case of HS, intensities of transitions are weak except for LU \rightarrow HO transition, since hot carriers relax much faster to frontier orbitals than that of LS and IS. Note that a recent study reveals that Redfield PL tends to narrow down the linewidth and blueshifts transition energies.⁵⁶

In summary, the ground state electronic properties of Fe-MMT under various spin multiplicities are explored utilizing spin-polarized DFT calculations with PBE functionals. HS is found with the lowest total energy in agreement with Hund's rule. With increasing spin multiplicities, one finds the increase of average distances between Fe and six nearest neighboring

O atoms. The VB edge of MMT is mainly contributed by O 2p, whereas the CB edge is by s orbitals of the host. From LS to HS, there is a shifting of Fe 3d states for spin α components toward the VB edge of MMT, while the corresponding spin β components remain almost unchanged. The substantial differences are due to their partial occupations. We also study the nonradiative and radiative relaxation channels of charge carriers by computing NACs using RDM approach with the Redfield formalism. Focusing on nonradiative relaxation of spin β components, the hole relaxation is found faster than the electron. With increasing spin multiplicities, one also finds the increase of both electron and hole relaxation rates. The hot electron relaxation in space is similar for various spin multiplicities. By contrast, the hot hole relaxation reveals different patterns. The distinct relaxation pathways in space and on time scale of photoinduced carriers suggest HS is suitable for photocatalytic applications. Focusing on radiative relaxation of spin β components, the Redfield PL spectra reveal obvious Fe 3d-3d transitions for LS and IS. The only intense PL peak for HS is Fe 3d to O 2p transition from LU to HO.

Supporting Information: computational details, interatomic distances of Fe and neighboring O, absorption spectra of spin α , nonradiative relaxation channels of spin α , detailed report on time-resolved and time-integrated PL spectra along excited state dynamics of spin α and spin β for LS, IS, and HS.

ACKNOLWEDGEMENT

This research was supported by the National Science Foundation (NSF) under NSF OIA ND-ACES Award No. 1946202. S.G. and W.X. acknowledged the support from the North Dakota Established Program to Stimulate Competitive Research (ND EPSCoR) through the New Faculty

Award, the Department of Civil, Construction and Environmental Engineering, and the College of Engineering at North Dakota State University (NDSU). S.G. acknowledged the Cyberinfrastructure Assistantship Award from ND EPSCoR. Department of Energy, DESC0022239, for research of light emitters based on earth abundant metals is acknowledged by authors. This work used supercomputing resources of DOE BES NERSC facility.

References

- (1) Feng, S.-S.; Mei, L.; Anitha, P.; Gan, C. W.; Zhou, W. Poly (Lactide)–Vitamin E Derivative/Montmorillonite Nanoparticle Formulations for the Oral Delivery of Docetaxel. *Biomaterials* **2009**, *30* (19), 3297–3306.
- (2) Peng, K.; Fu, L.; Yang, H.; Ouyang, J. Perovskite LaFeO 3/Montmorillonite Nanocomposites: Synthesis, Interface Characteristics and Enhanced Photocatalytic Activity. *Sci. Rep.* **2016**, *6* (1), 1–10.
- (3) Sun, S.; Wang, W.; Jiang, D.; Zhang, L.; Li, X.; Zheng, Y.; An, Q. Bi 2 WO 6 Quantum Dot-Intercalated Ultrathin Montmorillonite Nanostructure and Its Enhanced Photocatalytic Performance. *Nano Res.* **2014**, *7* (10), 1497–1506.
- (4) Arancibia-Miranda, N.; Baltazar, S. E.; García, A.; Muñoz-Lira, D.; Sepúlveda, P.; Rubio, M. A.; Altbir, D. Nanoscale Zero Valent Supported by Zeolite and Montmorillonite: Template Effect of the Removal of Lead Ion from an Aqueous Solution. *J. Hazard. Mater.* **2016**, *301*, 371–380.
- (5) Patel, H. A.; Somani, R. S.; Bajaj, H. C.; Jasra, R. V. Nanoclays for Polymer Nanocomposites, Paints, Inks, Greases and Cosmetics Formulations, Drug Delivery Vehicle and Waste Water Treatment. *Bull. Mater. Sci.* **2006**, *29* (2), 133–145.
- (6) Rong, N.; Chen, C.; Ouyang, K.; Zhang, K.; Wang, X.; Xu, Z. Adsorption Characteristics of Directional Cellulose Nanofiber/Chitosan/Montmorillonite Biomimetic Aerogel as Adsorbent for Wastewater Treatment. *Sep. Purif. Technol.* **2021**, 1–13.
- (7) Emam, E. A. Clays as Catalysts in Petroleum Refining Industry. *ARPN J. Sci. Technol.* **2013**, *3* (4), 356–375.
- (8) Man-Chao, H.; Zhi-Jie, F.; Ping, Z. Atomic and Electronic Structures of Montmorillonite in Soft Rock. *Chinese Phys. B* **2009**, *18* (7), 2933–2937.
- (9) Bergaya, F.; Lagaly, G. General Introduction: Clays, Clay Minerals, and Clay Science. *Dev. clay Sci.* **2006**, *1*, 1–18.
- (10) Akalin, E.; Akyuz, S.; Akyuz, T. Adsorption and Interaction of 5-Fluorouracil with Montmorillonite and Saponite by FT-IR Spectroscopy. *J. Mol. Struct.* **2007**, *834*, 477–481.
- (11) Jha, A.; Garade, A. C.; Shirai, M.; Rode, C. V. Metal Cation-Exchanged Montmorillonite Clay as Catalysts for Hydroxyalkylation Reaction. *Appl. Clay Sci.* **2013**, *74*, 141–146.
- (12) Zhang, D.; Zhou, C.-H.; Lin, C.-X.; Tong, D.-S.; Yu, W.-H. Synthesis of Clay Minerals. *Appl. Clay Sci.* **2010**, *50* (1), 1–11.
- (13) Uddin, F. Montmorillonite: An Introduction to Properties and Utilization; IntechOpen London, 2018.
- (14) Sainz-Díaz, C. I.; Palin, E. J.; Hernández-Laguna, A.; Dove, M. T. Octahedral Cation Ordering of Illite and Smectite. Theoretical Exchange Potential Determination and Monte Carlo Simulations. *Phys. Chem. Miner.* **2003**, *30* (6), 382–392.
- (15) Hernández-Laguna, A.; Escamilla-Roa, E.; Timon, V.; Dove, M. T.; Sainz-Díaz, C. I. DFT Study of the Cation Arrangements in the Octahedral and Tetrahedral Sheets of Dioctahedral 2: 1 Phyllosilicates. *Phys. Chem. Miner.* **2006**, *33* (10), 655–666.
- (16) Sainz-Díaz, C. I.; Palin, E. J.; Dove, M. T.; Hernández-Laguna, A. Monte Carlo Simulations of Ordering of Al, Fe, and Mg Cations in the Octahedral Sheet of Smectites and Illites. *Am. Mineral.* **2003**, *88* (7), 1033–1045.
- (17) Mignon, P.; Ugliengo, P.; Sodupe, M.; Hernandez, E. R. Ab Initio Molecular Dynamics Study of the Hydration of Li+, Na+ and K+ in a Montmorillonite Model. Influence of Isomorphic Substitution. *Phys. Chem. Chem. Phys.* **2010**, *12* (3), 688–697.
- (18) Polubesova, T.; Chen, Y.; Navon, R.; Chefetz, B. Interactions of Hydrophobic Fractions of Dissolved Organic Matter with Fe3+-and Cu2+-Montmorillonite. *Environ. Sci. Technol.* **2008**, *42* (13), 4797–4803.
- (19) Bérend, I.; Cases, J. M.; FranÃ, M. Ois, JP Uriot, LJ Michot, A. Masion and F. Thomas. Mechanism of Adsorption and Desorption of Water Vapor by Homoionic Montmorillonites: 2. the Li+, Na+,

- K+, Rb+, and Cs+ Exchanged Forms. *Clays Clay Miner.* **1995**, *43*, 324–336.
- (20) Cases, J. M.; Bérend, I.; Besson, G.; Francois, M.; Uriot, J. P.; Thomas, F.; Poirier, J. E. Mechanism of Adsorption and Desorption of Water Vapor by Homoionic Montmorillonite. 1. The Sodium-Exchanged Form. *Langmuir* **1992**, *8* (11), 2730–2739.
- (21) Fan, Y.-Q. Cation Diffusion and Conduction in Solid Electrolytes Li, Na-Montmorillonites. *Solid State Ionics* **1988**, *28*, 1596–1601.
- (22) Kohn, W.; Sham, L. J. Self-Consistent Equations Including Exchange and Correlation Effects. *Phys. Rev.* **1965**, *140* (4A), A1133–A1138.
- (23) Hohenberg, P.; Kohn, W. Inhomogeneous Electron Gas. Phys. Rev. 1964, 136 (3B), B864.
- (24) Wungu, T. D. K.; Aspera, S. M.; David, M. Y.; Dipojono, H. K.; Nakanishi, H.; Kasai, H. Absorption of Lithium in Montmorillonite: A Density Functional Theory (DFT) Study. *J. Nanosci. Nanotechnol.* **2011**, *11* (4), 2793–2801.
- (25) Pirillo, S.; Luna, C. R.; Lopez-Corral, I.; Juan, A.; Avena, M. J. Geometrical and Electronic Properties of Hydrated Sodium Montmorillonite and Tetracycline Montmorillonite from DFT Calculations. *J. Phys. Chem. C* **2015**, *119* (28), 16082–16088.
- (26) Peng, C.; Min, F.; Liu, L.; Chen, J. A Periodic DFT Study of Adsorption of Water on Sodium-Montmorillonite (001) Basal and (010) Edge Surface. *Appl. Surf. Sci.* **2016**, *387*, 308–316.
- (27) Zhao, J.; Cao, Y.; Wang, L.; Zhang, H.-J.; He, M.-C. Investigation on Atomic Structure and Mechanical Property of Na-and Mg-Montmorillonite under High Pressure by First-Principles Calculations. *Minerals* **2021**, *11* (6), 613.
- (28) Shafei, L.; Adhikari, P.; Ching, W.-Y. DFT Study of Electronic Structure and Optical Properties of Kaolinite, Muscovite, and Montmorillonite. *Crystals* **2021**, *11* (6), 1–10.
- (29) Perdew, J. P.; Burke, K.; Ernzerhof, M. Generalized Gradient Approximation Made Simple. *Phys. Rev. Lett.* **1996**, 77 (18), 3865–3868.
- (30) Yao, G.; Berry, M. T.; May, P. S.; Kilin, D. DFT Calculation of Russell–Saunders Splitting for Lanthanide Ions Doped in Hexagonal (β)-NaYF4 Nanocrystals. *J. Phys. Chem. C* **2013**, *117* (33), 17177–17185.
- (31) Micha, D. A.; Leathers, A. S. Reduced Density Matrix Equations for Combined Instantaneous and Delayed Dissipation in Many-Atom Systems, and Their Numerical Treatment. In *Energy Transfer Dynamics in Biomaterial Systems*; Springer, 2009; pp 363–380.
- (32) Vazhappilly, T.; Han, Y.; Kilin, D. S.; Micha, D. A. Electronic Relaxation of Photoexcited Open and Closed Shell Adsorbates on Semiconductors: Ag and Ag2 on TiO2. *J. Chem. Phys.* **2022**, *156* (10), 104705.
- (33) Redfield, A. G. On the Theory of Relaxation Processes. *IBM J. Res. Dev.* **1957**, 1 (1), 19–31.
- (34) Jean, J. M.; Friesner, R. A.; Fleming, G. R. Application of a Multilevel Redfield Theory to Electron Transfer in Condensed Phases. *J. Chem. Phys.* **1992**, *96* (8), 5827–5842.
- (35) Schmidt, S. R.; Katti, D. R.; Ghosh, P.; Katti, K. S. Evolution of Mechanical Response of Sodium Montmorillonite Interlayer with Increasing Hydration by Molecular Dynamics. *Langmuir* **2005**, *21* (17), 8069–8076.
- (36) Ghazanfari, S.; Faisal, H. M. N.; Katti, K. S.; Katti, D. R.; Xia, W. A Coarse-Grained Model for the Mechanical Behavior of Na-Montmorillonite Clay. *Langmuir* **2022**.
- (37) Perdew, J. P.; Chevary, J. A.; Vosko, S. H.; Jackson, K. A.; Pederson, M. R.; Singh, D. J.; Fiolhais, C. Atoms, Molecules, Solids, and Surfaces: Applications of the Generalized Gradient Approximation for Exchange and Correlation. *Phys. Rev. B* **1992**, *46* (11), 6671–6687.
- (38) Kresse, G.; Furthmüller, J. Efficiency of Ab-Initio Total Energy Calculations for Metals and Semiconductors Using a Plane-Wave Basis Set. *Comput. Mater. Sci.* **1996**, *6* (1), 15–50.
- (39) Kresse, G.; Hafner, J. Ab Initio Molecular Dynamics for Open-Shell Transition Metals. *Phys. Rev. B* **1993**, *48* (17), 13115–13118.
- (40) Ferreira, C. R.; Pulcinelli, S. H.; Scolfaro, L.; Borges, P. D. Structural and Electronic Properties of Iron-Doped Sodium Montmorillonite Clays: A First-Principles DFT Study. *ACS omega* **2019**, *4* (11), 14369–14377.

- (41) Tran, F.; Blaha, P. Accurate Band Gaps of Semiconductors and Insulators with a Semilocal Exchange-Correlation Potential. *Phys. Rev. Lett.* **2009**, *102* (22), 226401.
- (42) Heyd, J.; Scuseria, G. E.; Ernzerhof, M. Hybrid Functionals Based on a Screened Coulomb Potential. *J. Chem. Phys.* **2003**, *118* (18), 8207–8215.
- (43) Anisimov, V. I.; Zaanen, J.; Andersen, O. K. Band Theory and Mott Insulators: Hubbard U Instead of Stoner I. *Phys. Rev. B* **1991**, *44* (3), 943–954.
- Dudarev, S. L.; Botton, G. A.; Savrasov, S. Y.; Humphreys, C. J.; Sutton, A. P. Electron-Energy-Loss Spectra and the Structural Stability of Nickel Oxide: An LSDA+ U Study. *Phys. Rev. B* **1998**, 57 (3), 1505–1509.
- (45) Von Barth, U.; Hedin, L. A Local Exchange-Correlation Potential for the Spin Polarized Case. I. *J. Phys. C Solid State Phys.* **1972**, *5* (13), 1629–1642.
- (46) Kubler, J.; Hock, K.-H.; Sticht, J.; Williams, A. R. Density Functional Theory of Non-Collinear Magnetism. *J. Phys. F Met. Phys.* **1988**, *18* (3), 469–483.
- (47) Bulik, I. W.; Scalmani, G.; Frisch, M. J.; Scuseria, G. E. Noncollinear Density Functional Theory Having Proper Invariance and Local Torque Properties. *Phys. Rev. B* **2013**, *87* (3), 35117.
- (48) Yao, G.; Huang, S.; Berry, M. T.; May, P. S.; Kilin, D. S. Non-Collinear Spin DFT for Lanthanide Ions in Doped Hexagonal NaYF4. *Mol. Phys.* **2014**, *112* (3–4), 546–556.
- (49) Forde, A.; Inerbaev, T.; Hobbie, E. K.; Kilin, D. S. Excited-State Dynamics of a CsPbBr3 Nanocrystal Terminated with Binary Ligands: Sparse Density of States with Giant Spin–Orbit Coupling Suppresses Carrier Cooling. *J. Am. Chem. Soc.* **2019**, *141* (10), 4388–4397.
- (50) Han, Y.; Meng, Q.; Rasulev, B.; May, P. S.; Berry, M. T.; Kilin, D. S. Photoinduced Charge Transfer versus Fragmentation Pathways in Lanthanum Cyclopentadienyl Complexes. *J. Chem. Theory Comput.* **2017**, *13* (9), 4281–4296.
- (51) Inerbaev, T. M.; Hoefelmeyer, J. D.; Kilin, D. S. Photoinduced Charge Transfer from Titania to Surface Doping Site. *J. Phys. Chem. C* **2013**, *117* (19), 9673–9692.
- (52) Jensen, S. J.; Inerbaev, T. M.; Kilin, D. S. Spin Unrestricted Excited State Relaxation Study of Vanadium (IV)-Doped Anatase. *J. Phys. Chem. C* **2016**, *120* (11), 5890–5905.
- (53) Blöchl, P. E. Projector Augmented-Wave Method. *Phys. Rev. B* **1994**, *50* (24), 17953–17979.
- (54) Chu, W.; Zheng, Q.; Akimov, A. V; Zhao, J.; Saidi, W. A.; Prezhdo, O. V. Accurate Computation of Nonadiabatic Coupling with Projector Augmented-Wave Pseudopotentials. *J. Phys. Chem. Lett.* **2020**, *11* (23), 10073–10080.
- (55) Kasha, M. Characterization of Electronic Transitions in Complex Molecules. *Discuss. Faraday Soc.* **1950**, *9*, 14–19.
- (56) Inerbaev, T. M.; Han, Y.; Bekker, T. B.; Kilin, D. S. Mechanisms of Photoluminescence in Copper-Containing Fluoride Borate Crystals. *J. Phys. Chem. C* **2022**, 6119–6128.

Table and Figures

Table 1. Charge carrier relaxation rates related to **Figure 3** together with the oscillator strengths and transition energies for initial transitions.

Spin	Initial condition	Transition energy (eV)	Oscillator strength	$k_{\rm e},{\rm ps}^{{\scriptscriptstyle -1}}$	k_h , ps ⁻¹
LS	HO-15→LU+3	6.162	4.2018	0.0345	0.1473
IS	HO-14→LU+4	6.143	3.3243	0.1292	0.1857
HS	HO-13→LU+5	6.139	4.5063	0.2047	5.2758

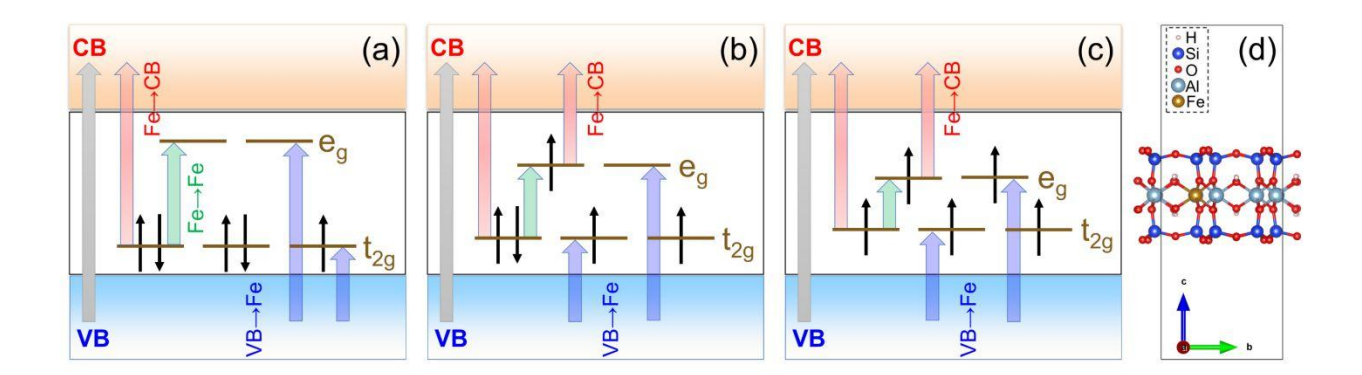


Figure 1. Simplified schematic band diagram of Fe³⁺-MMT under (a) LS, (b) IS, and (c) HS. (d) Optimized geometry of Fe-MMT for HS.

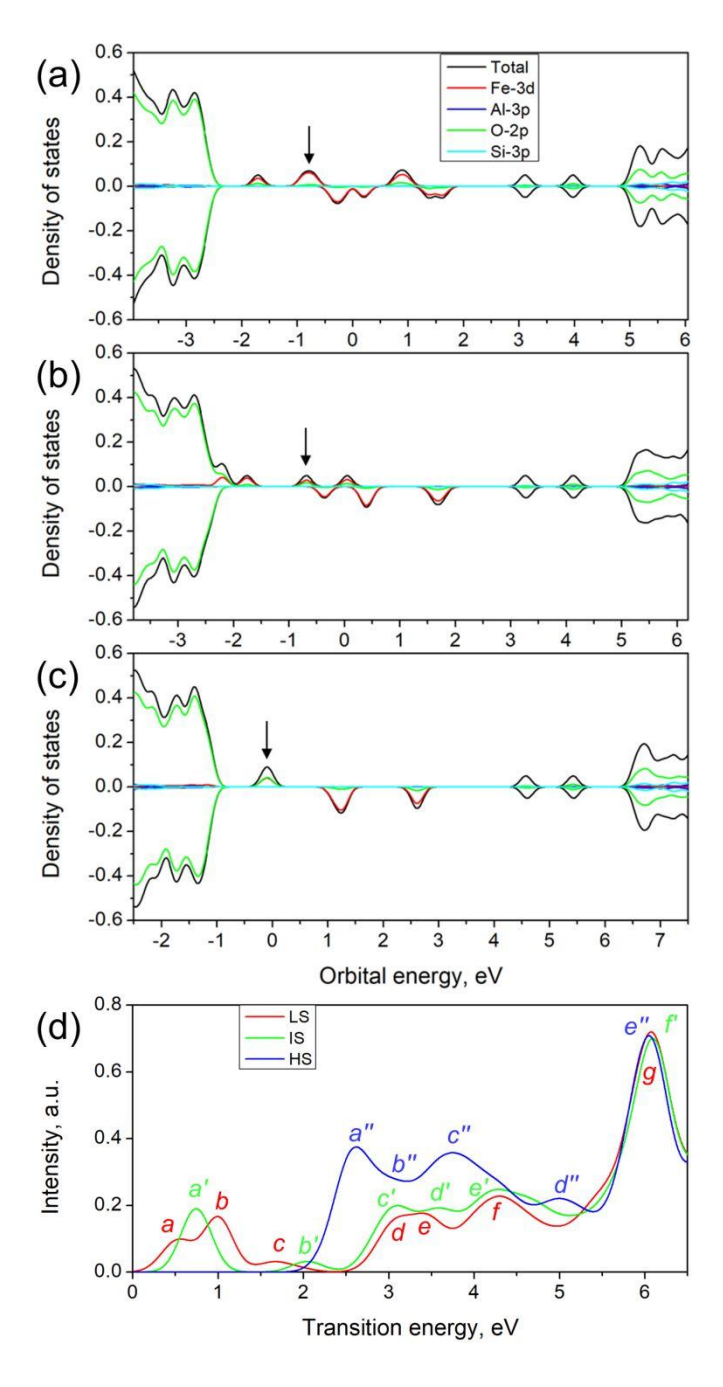


Figure 2. Partial density of states (a-c) and calculated spin β absorption spectra (d) for various spin multiplicities. (a) LS, (b) IS, (c) HS. The black arrows point to the location of HO orbitals in spin α. In PDOS, the zero energy refers to the Fermi level, which is defined as the midpoint between HO and LU in spin β . In panel (d), features a-g, a'-f', and a"-e" correspond to LS, IS, and HS, respectively.

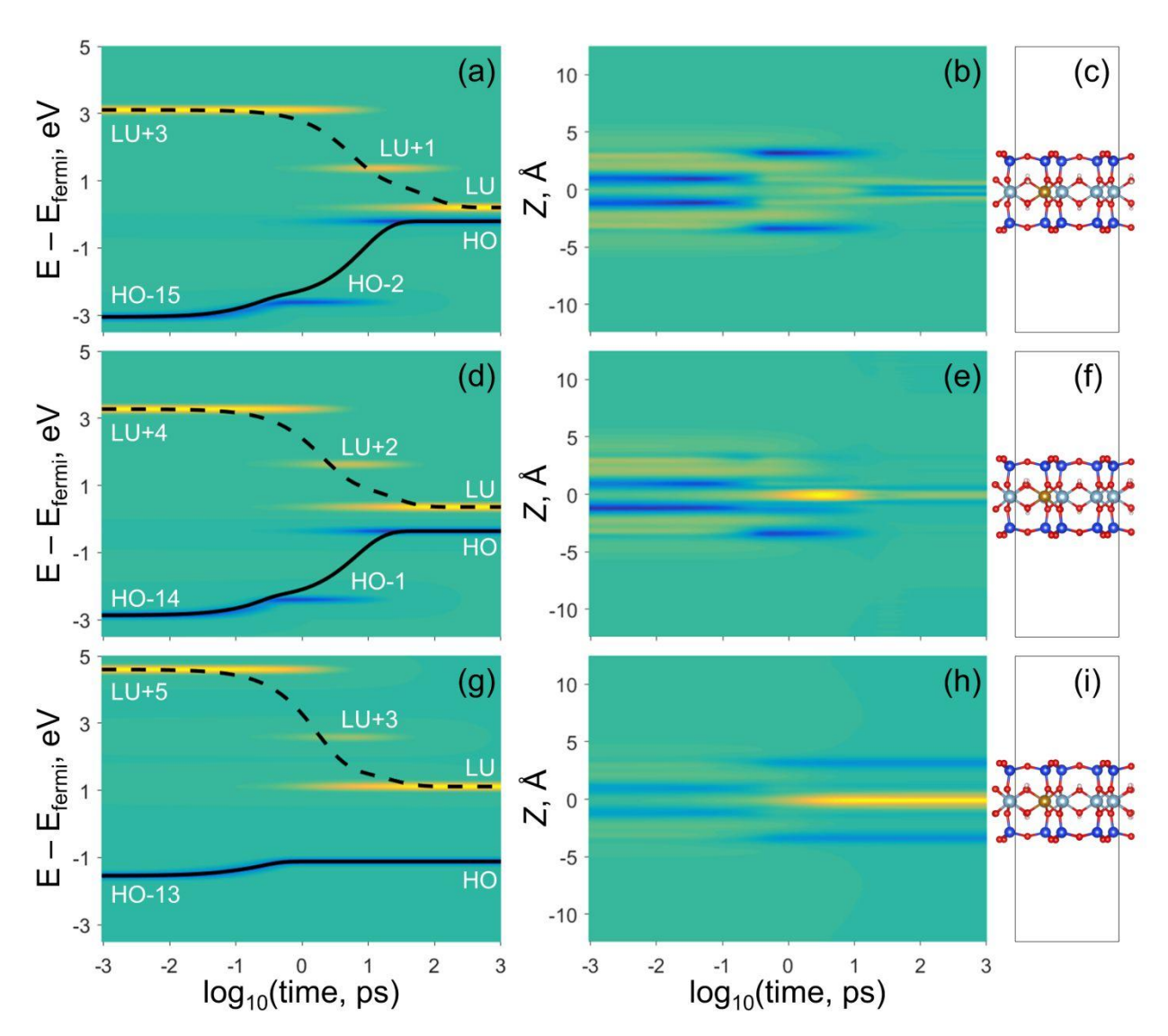


Figure 3. Charge carrier dynamics of Fe-MMT spin β for (a-c) LS, (d-f) IS, and (g-i) HS. In left and middle panels, green, yellow, and blue colors represent the equilibrium distribution, gain of electron density, and loss of electron density, respectively. The black dotted and solid lines represent energy expectation values of electrons and holes, respectively. The left panels show isocontours of population density changes as a function of energy and time. The middle panels show isocontours of population density changes as a function of z-projection and time. The right panels show optimized structures, which are scaled to match with the middle panels.

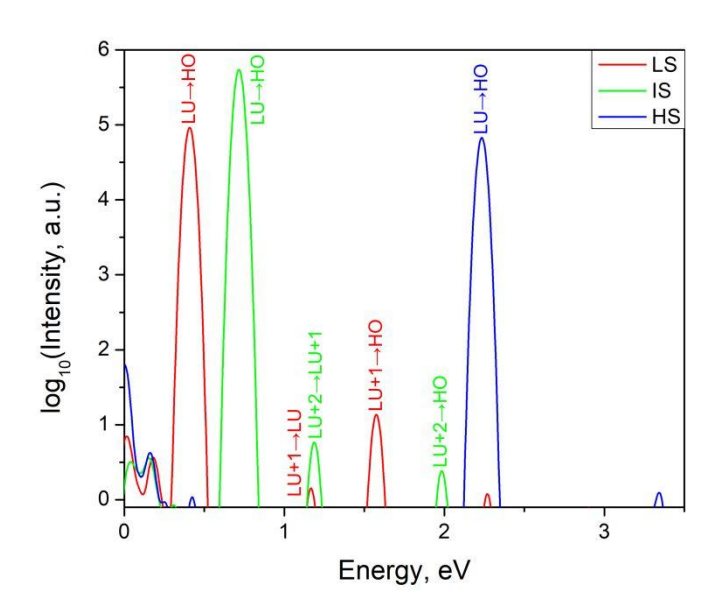


Figure 4. Time-integrated emission spectra along the excited-state trajectories of Fe-MMT spin β for LS (red), IS (green) and HS (blue). The initial photoexcitation conditions are the same as those in **Figure 3**.